


MATERIALS SCIENCE

Decoupling engineering of formamidinium–cesium perovskites for efficient photovoltaics

Haoran Chen^{1,†}, Yong Wang^{2,†}, Yingping Fan^{1,†}, Yuetian Chen¹ , Yanfeng Miao¹, Zhixiao Qin¹, Xingtao Wang¹, Xiaomin Liu¹, Kaicheng Zhu¹, Feng Gao^{2,*} and Yixin Zhao^{1,3,*}

ABSTRACT

Although pure formamidinium iodide perovskite (FAPbI₃) possesses an optimal gap for photovoltaics, their poor phase stability limits the long-term operational stability of the devices. A promising approach to enhance their phase stability is to incorporate cesium into FAPbI₃. However, state-of-the-art formamidinium–cesium (FA–Cs) iodide perovskites demonstrate much worse efficiency compared with FAPbI₃, limited by the different crystallization dynamics of formamidinium and cesium, which result in poor composition homogeneity and high trap densities. We develop a novel strategy of crystallization decoupling processes of formamidinium and cesium via a sequential cesium incorporation approach. As such, we obtain highly reproducible, highly efficient and stable solar cells based on FA_{1-x}Cs_xPbI₃ ($x = 0.05–0.16$) films with uniform composition distribution in the nanoscale and low defect densities. We also revealed a new stabilization mechanism for Cs doping to stabilize FAPbI₃, i.e. the incorporation of Cs into FAPbI₃ significantly reduces the electron–phonon coupling strength to suppress ionic migration, thereby improving the stability of FA–Cs-based devices.

Keywords: formamidinium–cesium, perovskite solar cell, decoupling engineering, sequential cesium incorporation, uniform composition distribution

INTRODUCTION

Metal–halide perovskites with superior photophysical properties and low-cost solution technology have emerged as promising candidates for different optoelectronic devices, including solar cells, light-emitting diodes, etc. [1–6]. For perovskite solar cells (PSCs), the certified power-conversion efficiency (PCE) has reached 25.7%, which is comparable to the current commercial crystalline silicon solar cells. ABX₃ perovskites with tailoring compositions, where A is an organic or inorganic cation, B is a metal cation and X is a halide anion, have been attempted for high efficiency and stable photovoltaic devices. Among these, formamidinium lead iodide (FAPbI₃) has exhibited great potential as the absorber layer, due to its optimal band gap of ~1.5 eV and excellent thermal stability [7–9].

However, the photoactive FAPbI₃ black phase would easily transform into a non-photoactive yel-

low δ -FAPbI₃ phase at room temperature, especially under humid conditions [10,11]. The poor phase stability challenges both the efficiency and long-term stability of the PSCs based on FAPbI₃ [12,13]. It is generally believed that the phase instability of FAPbI₃ perovskites originates from its unsuitable tolerant factor. To address this problem, alloying FA⁺ with MA⁺/Cs⁺ cations or partially substituting I⁻ with Br⁻ ions has been employed to tune the tolerant factor [14,15]. The resulting mixed-ion FA-based perovskites exhibit improved resistance to phase transition.

Among these different alloying approaches, formamidinium–cesium mixed-cation pure iodide (FA_{1-x}Cs_xPbI₃) perovskites are particularly promising, because they avoid the concerns about volatile MA cations and phase segregation induced by mixed halide ions (Br–I) [16–20]. However, because of the complex crystallization kinetics of

¹School of Environmental Science and Engineering, Frontiers Science Center for Transformative Molecules, Shanghai Jiao Tong University, Shanghai 200240, China; ²Department of Physics, Chemistry and Biology (IFM), Linköping University, Linköping 58183, Sweden and ³Shanghai Institute of Pollution Control and Ecological Security, Shanghai 200240, China

*Corresponding authors. E-mails: yixin.zhao@sjtu.edu.cn; feng.gao@liu.se

[†]Equally contributed to this work.

Received 8 March 2022; Revised 25 May 2022; Accepted 19 June 2022

formamidinium and cesium, these pure iodide FA–Cs perovskites fabricated by one-step crystallization suffer from poor composition homogeneity and high defects/traps densities [21,22]. The PSCs based on these films are therefore facing relatively low efficiencies. Especially, strong non-radiative recombination in all reported FA–Cs-based PSCs limited the open-circuit voltage (V_{oc}) of the resulting devices [23–25].

Herein, we develop a novel sequential Cs incorporation (SCI) strategy to decouple the crystallization processes of formamidinium and cesium, and achieve highly efficient pure iodide $FA_{1-x}Cs_xPbI_3$ ($x = 0.05–0.16$) perovskites (denoted as SCI- $FA_{1-x}Cs_xPbI_3$). The ratio of FA and Cs in $FA_{1-x}Cs_xPbI_3$ can be straightforwardly tuned by introducing different concentrations of cesium formate (HCOOCs) solution on the FA-based perovskite precursor film during the SCI process. A unique feature of our SCI- $FA_{1-x}Cs_xPbI_3$ perovskites is the uniform distributions of Cs cations, in contrast to their poor uniformity in typical one-step (1S) crystallized FA–Cs perovskite films (denoted as 1S- $FA_{1-x}Cs_xPbI_3$). As a result, the champion SCI- $FA_{0.91}Cs_{0.09}PbI_3$ PSCs yield a record PCE of 24.7% (certified 23.8%) with improved V_{oc} and fill factor, which is the highest value for the pure iodide $FA_{1-x}Cs_xPbI_3$ perovskites. Compared with FAPbI₃, the SCI- $FA_{0.91}Cs_{0.09}PbI_3$ perovskite shows reduced electron–phonon coupling and lattice fluctuations, which suppress the formation of iodide-rich clusters and finally contribute to the excellent operational stability of the $FA_{0.91}Cs_{0.09}PbI_3$ -based PSCs.

RESULT AND DISCUSSION

Figure 1a shows the schematic diagram of SCI- $FA_{1-x}Cs_xPbI_3$ perovskite films prepared by decoupling the crystallization processes of formamidinium and cesium. A FAPbI₃ precursor film was first deposited by a typical anti-solvent method followed by annealing for 1 min. The Cs cation is sequentially introduced onto the FA perovskite film by spin-coating HCOOCs isopropanol (IPA) solution, followed by further annealing. For comparison, we employed different concentrations of HCOOCs solution (2.5, 5 and 10 mg mL⁻¹) to fabricate SCI- $FA_{1-x}Cs_xPbI_3$ perovskites. The final ratios of incorporated Cs in the above SCI- $FA_{1-x}Cs_xPbI_3$ perovskite films, i.e. the value of x , are 0.05, 0.09 and 0.16, as confirmed by inductively coupled plasma–mass spectrometry (ICP–MS) analysis (Supplementary Table 1). The corresponding SCI- $FA_{1-x}Cs_xPbI_3$ perovskite films are noted as $x = 0.05$, $x = 0.09$ and $x = 0.16$ in Fig. 1.

Optical and structural measurements of perovskite films indicate that Cs⁺ from HCOOCs has successfully been incorporated into the lattice of FAPbI₃ perovskites. Figure 1b shows the ultraviolet–visible (UV–vis) spectra of SCI- $FA_{1-x}Cs_xPbI_3$ perovskite films, in which the absorption edges of SCI- $FA_{1-x}Cs_xPbI_3$ perovskites strongly depend on the amount of Cs⁺ incorporation. When x increases from 0 to 0.16, the absorption edges of SCI- $FA_{1-x}Cs_xPbI_3$ perovskites gradually blue-shift from 816 to 802 nm, and the corresponding photoluminescence (PL) peaks shift from 809 to 797 nm. The X-ray diffraction (XRD) measurements are carried out to investigate the crystal structure evolution of SCI- $FA_{1-x}Cs_xPbI_3$ perovskites (Fig. 1c). All the SCI- $FA_{1-x}Cs_xPbI_3$ perovskites exhibit stronger peak intensity than the pure FAPbI₃ at around both 14° and 28°, corresponding to (001) and (002) perovskite crystal planes. The inset image of Fig. 1c shows that the peak between 13.8° and 14.1° shifts to a higher degree, indicating that Cs ions are incorporated into the perovskite lattice. The lattice parameter decreases with increasing the amount of Cs (Supplementary Fig. 1), further confirming the successful mixing of Cs⁺ in the perovskite lattice. The tolerance factor of SCI- $FA_{1-x}Cs_xPbI_3$ perovskites is also reduced compared with pure FA perovskite, potentially contributing to a stable perovskite structure (Supplementary Fig. 2).

The Cs incorporation also significantly improves the film morphologies (Fig. 1d). All SCI- $FA_{1-x}Cs_xPbI_3$ films show enlarged and pinhole-free grains compared with the FAPbI₃ film, which shows coarse grains and pinholes. As shown in the cross-sectional scanning electron microscopy (SEM) images, SCI- $FA_{1-x}Cs_xPbI_3$ perovskite films (550–600 nm) with vertical growth of grains benefit efficient charge extraction.

By adopting these Cs-incorporated perovskites as light absorber layers, we fabricate PSCs with a configuration of fluorine-doped tin oxide (FTO)/electron-transport layer/perovskite/hole-transport layer/Au. All SCI- $FA_{1-x}Cs_xPbI_3$ ($x = 0.05, 0.09, 0.16$)-based PSCs exhibit improved device efficiency compared with the FAPbI₃-based devices (Supplementary Fig. 3). Considering that $x = 0.09$ provides the optimal photovoltaic (PV) performance, we then chose this composition (denoted as SCI- $FA_{0.91}Cs_{0.09}PbI_3$) for detailed investigations on Cs incorporation and its role on film and device properties.

X-ray photoelectron spectroscopy spectra are conducted to explore the effect of SCI on the elements and their chemical states in perovskite films. All core-level peaks are assigned to Cs, Pb,

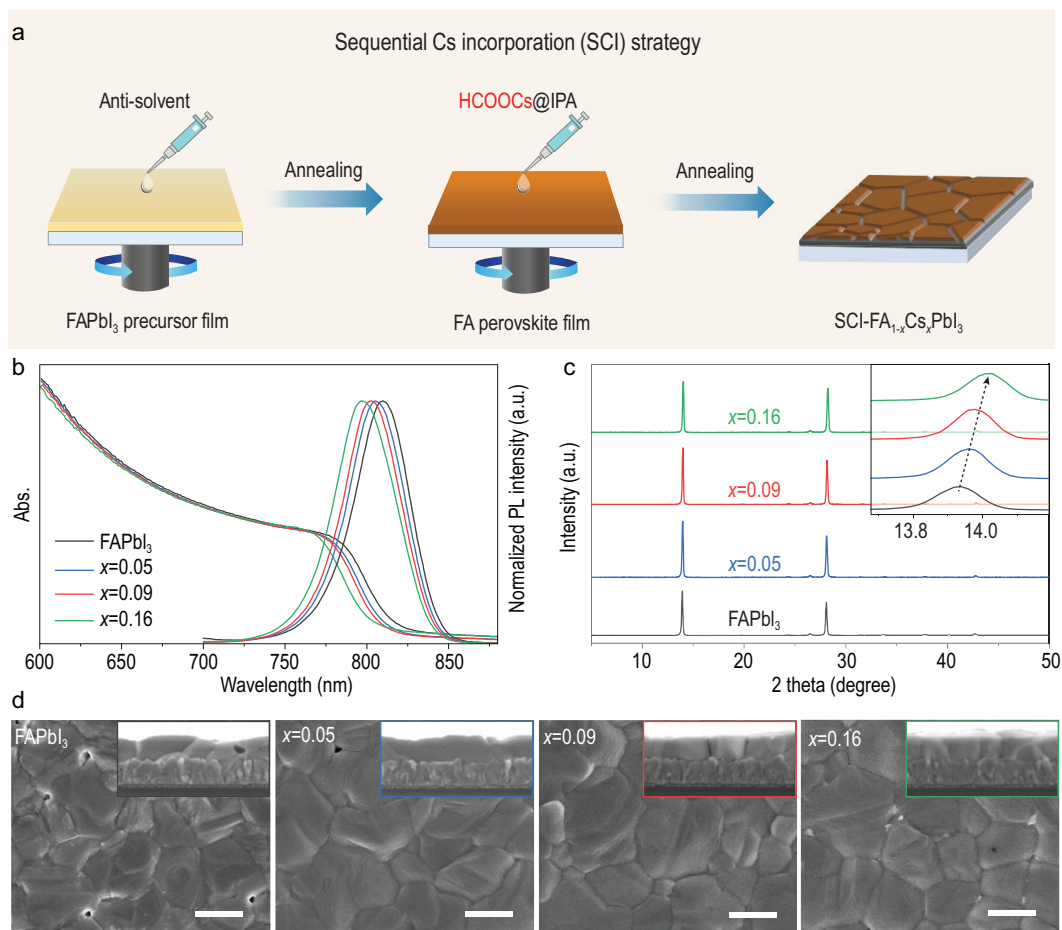


Figure 1. Spectroscopic, structural and morphological characterizations of SCI-FA_{1-x}Cs_xPbI₃ films. (a) Schematic diagram of the SCI-FA_{1-x}Cs_xPbI₃ perovskite films fabricated by decoupling the crystallization processes of formamidinium and cesium. (b) UV-vis absorption and normalized PL spectra and (c) XRD patterns of FAPbI₃ and SCI-FA_{1-x}Cs_xPbI₃ perovskites. Inset pattern corresponding to the characteristic peaks of (001) perovskite crystal planes. (d) Top-surface SEM images of FAPbI₃ and SCI-FA_{1-x}Cs_xPbI₃ perovskite films. The inset presents the cross-sectional morphology of the corresponding perovskite films. Scale bars: 1 μ m.

N and I (Supplementary Fig. 4) elements. The characteristic Cs signals in the SCI-FA_{0.91}Cs_{0.09}PbI₃ perovskite locate at 738.5 and 724.7 eV, and show a 1.1-eV shift compared with the Cs in HCOOCs. Such a large shift is attributed to the formation of chemical bonds between Cs⁺ and [PbI₆]⁴⁻. For the Pb 4f spectra in FAPbI₃, two peaks corresponding to Pb 4f_{7/2} and Pb 4f_{5/2} are observed at 138.3 and 143.2 eV. However, in the SCI-FA_{0.91}Cs_{0.09}PbI₃ perovskite, both Pb 4f_{7/2} and Pb 4f_{5/2} shift by 0.1 eV toward higher binding energy, originating from the stronger bond energies between Cs⁺ and [PbI₆]⁴⁻ than that between FA⁺ and [PbI₆]⁴⁻. Additionally, the N and I elements representing the formamidinium component have undergone a small shift. These results further confirm that Cs has been successfully incorporated into the FAPbI₃ perovskite lattice to form SCI-FA_{0.91}Cs_{0.09}PbI₃ perovskite.

For comparison, we also fabricate one-step crystallized 1S-FA_{1-x}Cs_xPbI₃, where Cs⁺ (from

HCOOCs) is directly mixed with FA⁺ in the perovskite precursor. For 1S-FA_{1-x}Cs_xPbI₃ PSCs (Supplementary Fig. 5), the optimal efficiency is also obtained from the $x = 0.09$ sample, which hence will be used as the control sample for comparison with SCI-FA_{0.91}Cs_{0.09}PbI₃. The absorption edge, characteristic XRD peaks and surface morphologies of the 1S-FA_{0.91}Cs_{0.09}PbI₃ perovskite films are consistent with SCI-FA_{0.91}Cs_{0.09}PbI₃ perovskite (Supplementary Fig. 6).

The synchrotron-based grazing-incidence wide-angle X-ray scattering (GIWAXS) and time-of-flight secondary ion mass spectrometry (ToF-SIMS) measurements are further employed to explore the crystal structure and internal composition in perovskite films. As shown in Fig. 2a and b, there is a signal ring at $q_{xy} = 8.8 \text{ nm}^{-1}$ corresponding to δ -FAPbI₃ in 1S-FA_{0.91}Cs_{0.09}PbI₃ perovskite, while the GIWAXS result of SCI-FA_{0.91}Cs_{0.09}PbI₃ exhibits high phase purity and obvious crystal orientation

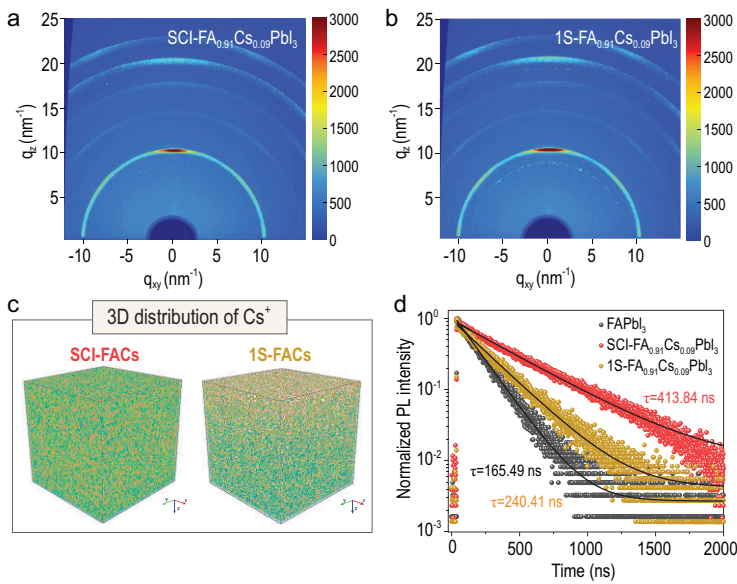


Figure 2. Characterizations of $\text{FA}_{0.91}\text{Cs}_{0.09}\text{PbI}_3$ perovskite films. GIWAXS data of (a) $\text{SCI-FA}_{0.91}\text{Cs}_{0.09}\text{PbI}_3$ and (b) $\text{1S-FA}_{0.91}\text{Cs}_{0.09}\text{PbI}_3$ films. (c) 3D distribution in the $\text{SCI-FA}_{0.91}\text{Cs}_{0.09}\text{PbI}_3$ and $\text{1S-FA}_{0.91}\text{Cs}_{0.09}\text{PbI}_3$ film by ToF-SIMS analysis, where the signal intensity in two kinds of perovskites is normalized. (d) TRPL decay curves of FAPbI_3 , $\text{SCI-FA}_{0.91}\text{Cs}_{0.09}\text{PbI}_3$ and $\text{1S-FA}_{0.91}\text{Cs}_{0.09}\text{PbI}_3$ perovskite films.

without any obvious phase impurities. Since the distribution of Cs in $\text{SCI-FA}_{1-x}\text{Cs}_x\text{PbI}_3$ perovskite has a significant effect on both the phase stability and traps/defects [22,26], we proceed to investigate the distribution of Cs in the $\text{SCI-FA}_{0.91}\text{Cs}_{0.09}\text{PbI}_3$ and $\text{1S-FA}_{0.91}\text{Cs}_{0.09}\text{PbI}_3$ perovskites. Both energy-dispersive spectroscopy mapping and ToF-SIMS have established that the incorporated Cs^+ cations homogeneously distribute in the surface and bulk of $\text{SCI-FA}_{0.91}\text{Cs}_{0.09}\text{PbI}_3$ perovskite, which is completely different from the inhomogeneous Cs^+ cation distributions in $\text{1S-FA}_{0.91}\text{Cs}_{0.09}\text{PbI}_3$ perovskite (Fig. 2c and Supplementary Fig. 7). The Cs aggregation at the top surface of $\text{1S-FA}_{0.91}\text{Cs}_{0.09}\text{PbI}_3$ reveals the phase separation in $\text{1S-FA}_{0.91}\text{Cs}_{0.09}\text{PbI}_3$, which is consistent with the GIWAXS data. Such uniform distribution of Cs ions in the $\text{SCI-FA}_{0.91}\text{Cs}_{0.09}\text{PbI}_3$ perovskite originates from the decoupled crystallization kinetics by the SCI strategy, which is beneficial for enhancing the phase stability and reducing defects/traps density. Different from Cs^+ cations, other ions, including FA^+ , Pb^{2+} and I^- , are uniformly distributed throughout both the $\text{SCI-FA}_{0.91}\text{Cs}_{0.01}\text{PbI}_3$ and $\text{1S-FA}_{0.91}\text{Cs}_{0.09}\text{PbI}_3$ perovskite films (Supplementary Fig. 8). Although most of the HCOO^- anions escape from the $\text{FA}_{0.91}\text{Cs}_{0.09}\text{PbI}_3$ perovskite during the annealing process, residual traces of HCOO^- still exist at the bottom interface between the perovskite and the substrate (Supplementary Fig. 9), which can further passivate the defects

on the bottom interface and improve the charge carriers' dynamics in the devices [27,28].

Uniform incorporation of Cs ions into FAPbI_3 has two positive effects: enhanced phase stability and decreased trap/defect densities. The enhanced phase stability is evidenced from the absence of color/structural changes under humid conditions. Under 60% relative humidity, the $\text{SCI-FA}_{0.91}\text{Cs}_{0.09}\text{PbI}_3$ perovskite maintains the black phase for 7 days without any changes (Supplementary Fig. 10), showing significant improvement compared with FAPbI_3 . The decreased trap/defect densities are demonstrated from photophysical measurements. The photoluminescence (PL) intensities of $\text{SCI-FA}_{0.91}\text{Cs}_{0.09}\text{PbI}_3$ perovskites are much stronger than those of $\text{1S-FA}_{0.91}\text{Cs}_{0.09}\text{PbI}_3$ and pure FA perovskite films (Supplementary Fig. 11). In addition, the time-resolved PL (TRPL) spectra in Fig. 2d show that the PL lifetime (τ) of $\text{SCI-FA}_{0.91}\text{Cs}_{0.09}\text{PbI}_3$ is much longer (413.84 ns) than that of $\text{1S-FA}_{0.91}\text{Cs}_{0.09}\text{PbI}_3$ (240.41 ns) and FAPbI_3 (165.49 ns). Enhanced PL intensity and improved PL lifetime indicate that non-radiative recombination is suppressed in $\text{SCI-FA}_{0.91}\text{Cs}_{0.09}\text{PbI}_3$, attributed to decreased trap densities. Consistently, we calculated the Urbach energy (E_u) according to the equation: $A = A_0 \exp(E/E_u)$, where A is the absorbance, A_0 is a constant for data fitting and E is the excitation energy. The Urbach energy (Supplementary Fig. 12) is decreased from 22.2 meV in FAPbI_3 and 21.6 meV in $\text{1S-FA}_{0.91}\text{Cs}_{0.09}\text{PbI}_3$ to 18.3 meV in $\text{SCI-FA}_{0.91}\text{Cs}_{0.09}\text{PbI}_3$. The smaller Urbach energy in $\text{SCI-FA}_{0.91}\text{Cs}_{0.09}\text{PbI}_3$ corresponds to a lower density of trap states. These results suggest that, with sequential incorporation of Cs^+ , the $\text{SCI-FA}_{0.91}\text{Cs}_{0.09}\text{PbI}_3$ perovskite exhibits significantly reduced non-radiative recombination via defects/traps.

Benefitting from these advantages of crystallization decoupling engineering, the resulting $\text{SCI-FA}_{0.91}\text{Cs}_{0.09}\text{PbI}_3$ perovskite shows much enhanced device performance. Figure 3a compares the current density–voltage (J – V) characteristics of champion PSCs based on FAPbI_3 , $\text{SCI-FA}_{0.91}\text{Cs}_{0.09}\text{PbI}_3$ and $\text{1S-FA}_{0.91}\text{Cs}_{0.09}\text{PbI}_3$ perovskites, respectively. The $\text{SCI-FA}_{0.91}\text{Cs}_{0.09}\text{PbI}_3$ -based PSC exhibits an impressive PCE of 24.7% compared with 22.6% for FAPbI_3 , representing a new record for pure iodide $\text{FA}_{1-x}\text{Cs}_x\text{PbI}_3$ -based PSCs (Supplementary Table 2). A certified PCE of 23.8% with negligible hysteresis has been obtained in the $\text{SCI-FA}_{0.91}\text{Cs}_{0.09}\text{PbI}_3$ -based PSCs (Supplementary Fig. 13). The most striking difference is the V_{oc} , which increases from 1.09 V in FAPbI_3 to 1.18 V in $\text{SCI-FA}_{0.91}\text{Cs}_{0.09}\text{PbI}_3$. The counterpart PSCs based on $\text{1S-FA}_{0.91}\text{Cs}_{0.09}\text{PbI}_3$ perovskite yield a

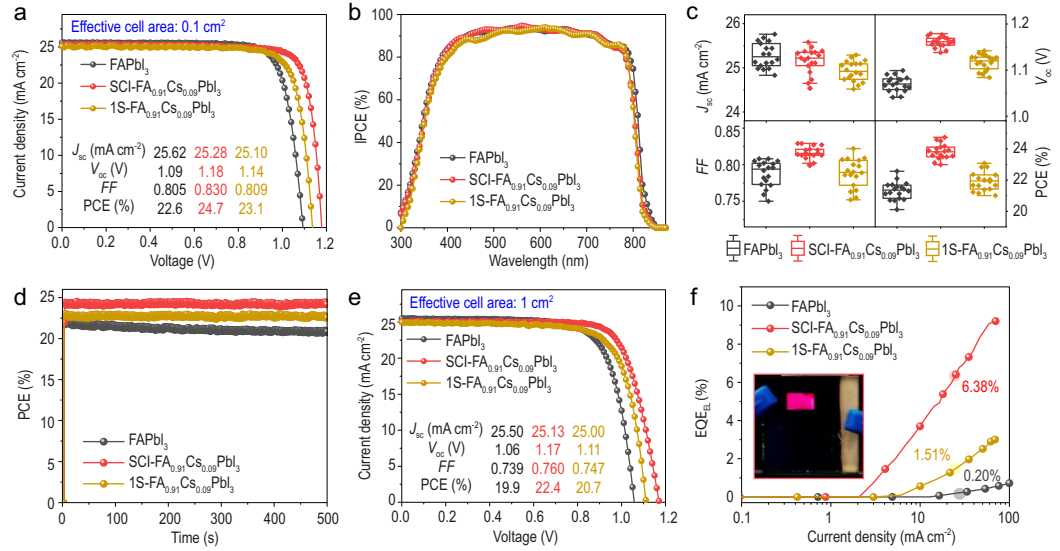


Figure 3. Photovoltaic and device characterization. (a) The J - V curves of the champion devices of FAPbI₃, SCI-FA_{0.91}Cs_{0.09}PbI₃ and 1S-FA_{0.91}Cs_{0.09}PbI₃ PSCs with 0.1 cm² of effective cell area. (b) IPCE spectra of FAPbI₃, SCI-FA_{0.91}Cs_{0.09}PbI₃- and 1S-FA_{0.91}Cs_{0.09}PbI₃-based PSCs. (c) The PV performance distribution of FAPbI₃-, SCI-FA_{0.91}Cs_{0.09}PbI₃- and 1S-FA_{0.91}Cs_{0.09}PbI₃-based PSCs from 18 devices, respectively. (d) Steady-state efficiency of FAPbI₃ and SCI-FA_{0.91}Cs_{0.09}PbI₃ and 1S-FA_{0.91}Cs_{0.09}PbI₃ PSCs. (e) J - V characteristics of PSCs based on FAPbI₃, SCI-FA_{0.91}Cs_{0.09}PbI₃ and 1S-FA_{0.91}Cs_{0.09}PbI₃ with 1 cm² of effective cell area under simulated AM 1.5-G solar illumination of 100 mW cm⁻² in the reverse scan. (f) EQE_{EL} of FAPbI₃-, SCI-FA_{0.91}Cs_{0.09}PbI₃- and 1S-FA_{0.91}Cs_{0.09}PbI₃-based PSCs vs. the current density.

lower efficiency of 23.1%. This comparison indicates that our crystallization decoupling engineering is beneficial for enhancing SCI-FA_{1-x}Cs_xPbI₃-based PSCs performance. The incident photon to electron conversion efficiency (IPCE) (Fig. 3b) is similar for both devices, with a high value of >90% in the wavelength range of 450–650 nm. The short-circuit current density (J_{sc}) of the SCI-FA_{0.91}Cs_{0.09}PbI₃ device is slightly decreased compared with the FAPbI₃ device, mainly due to slight increase in the band gap upon Cs incorporation. Figure 3c compares the PV parameters of FAPbI₃-, SCI-FA_{0.91}Cs_{0.09}PbI₃- and 1S-FA_{0.91}Cs_{0.09}PbI₃-based PSCs for 18 devices, respectively, indicating that sequential Cs incorporation also improves the device reproducibility. In addition, the SCI-FA_{0.91}Cs_{0.09}PbI₃-based PSCs exhibit a smaller hysteresis (Supplementary Figs 13 and 14), resulting in a stabilized output power of 24.4% (Fig. 3d).

In addition to small-area PSCs, the large-area PSCs based on these sequential Cs-incorporated perovskite films also exhibit significantly improved device performance. The champion SCI-FA_{0.91}Cs_{0.09}PbI₃ device, fabricated on 2.5 × 2.5 cm² substrates with an effective cell area of 1 cm² (Fig. 3e), displays a PCE of 22.4%, which is far higher than the FAPbI₃ (~19.9%) and 1S-FA_{0.91}Cs_{0.09}PbI₃ (~20.7%)-based devices.

The significantly enhanced V_{oc} of the SCI-FA_{0.91}Cs_{0.09}PbI₃ device is mainly due to suppressed

non-radiative recombination, which can be quantified by measuring the external quantum efficiency of electroluminescence (EQE_{EL}) values [29]. As shown in Fig. 3f, at the injection current densities corresponding to J_{sc} , the EQE_{EL} value of the SCI-FA_{0.91}Cs_{0.09}PbI₃ device is 6.38%, while that of the FAPbI₃ device is 0.16%. We calculate the voltage losses due to non-radiative recombination ($\Delta V_{oc, non-rad}$) based on the formula [30]:

$$\Delta V_{oc, non-rad} = -\frac{kT}{q} \ln EQE_{EL},$$

where k , T and q represent the Boltzmann constant, temperature and elementary electric charge, respectively. The difference in $\Delta V_{oc, non-rad}$ (0.09 V) matches well with the difference of device V_{oc} (0.09 V).

Suppressed non-radiative recombination in the SCI-FA_{0.91}Cs_{0.09}PbI₃ device is consistent with previous photophysical measurements on the films, which indicate that the sequential Cs incorporation can reduce the defects/traps. Further measurements on the devices also reach similar conclusions. The trap-filled limiting voltage in the space-charge limited current measurements decreases from 0.13 V in the FAPbI₃ device to 0.09 V in SCI-FA_{0.91}Cs_{0.09}PbI₃ device (Supplementary Fig. 15), indicating suppressed traps/defects upon Cs sequential incorporation [31,32]. These results are also consistent with transient photovoltage (TPV) decay and transient photocurrent (TPC) decay results (Supplementary

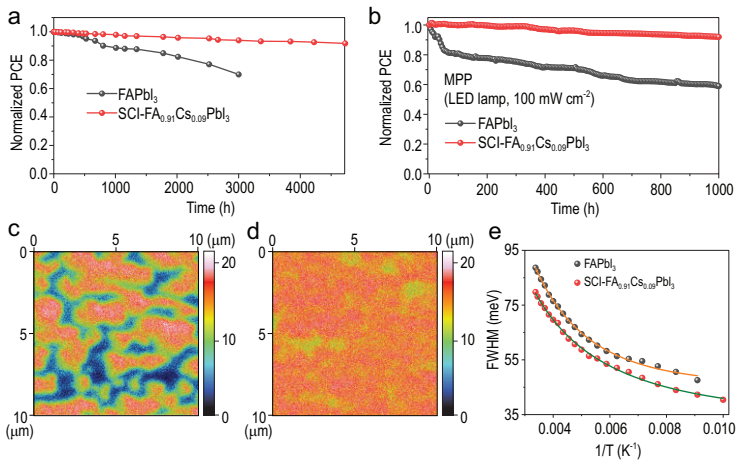


Figure 4. Stability of the SCI-FA_{0.91}Cs_{0.09}PbI₃ PSCs. (a) The shelf-life stability of unencapsulated FAPbI₃ and SCI-FA_{0.91}Cs_{0.09}PbI₃ PSCs. (b) The long-term operational stability of unencapsulated FAPbI₃ and SCI-FA_{0.91}Cs_{0.09}PbI₃ PSCs. The 2D I⁻ distribution in the middle of the perovskite layer (at ~300 nm) for PSCs based on (c) FAPbI₃ and (d) SCI-FA_{0.91}Cs_{0.09}PbI₃ perovskites after 240 h of operational stability test at their MPP by ToF-SIMS. (e) Fit of the FWHM of the PL spectra vs. temperature.

Fig. 16), which show slower TPV decay (indicating longer recombination lifetime) and quicker TPC decay (indicating fewer trapping effects) in the SCI-FA_{0.91}Cs_{0.09}PbI₃ device [33,34].

In addition to improved PV performance, the SCI-FA_{0.91}Cs_{0.09}PbI₃ device also shows significantly enhanced stability. We first measure the shelf life by storing the unencapsulated devices in dark at 25 °C and 20% relative humidity. Figure 4a shows that the PCE of the FAPbI₃ device decreases by ~30% after 3000 h of aging, whereas the SCI-FA_{0.91}Cs_{0.09}PbI₃ device shows a degradation of only 10% over 4500 h of aging. We then investigate the long-term operational stability of the PSCs by aging the unencapsulated devices under a nitrogen atmosphere, using maximum power point (MPP) tracking under simulated 1-sun conditions. As shown in Fig. 4b, the SCI-FA_{0.91}Cs_{0.09}PbI₃ based PSCs retains >90% of the initial PCE while the FAPbI₃ device maintains only 60% PCE after 1000 h of continuous illumination (Supplementary Fig. 17). Especially, the sharp decline of the efficiency in FAPbI₃ PSCs in the initial stage should be attributed to the intrinsic instability of the FAPbI₃ perovskite layer and potential severe ion migration in the FAPbI₃ device.

A main reason for enhanced-stability PSCs is attributed to suppressed ionic migration. In Fig. 4c and d, we compare the I⁻ ions distribution at the ~300-nm depth of the perovskite layer for PSCs based on FAPbI₃ and SCI-FA_{0.91}Cs_{0.09}PbI₃ after 240-h MPP test. In the FAPbI₃-based device, strong aggregation of I⁻ clusters is observed in the perovskite absorber layers; in contrast, I⁻ ions

distribute uniformly in the SCI-FA_{0.91}Cs_{0.09}PbI₃-based devices. This sharp contrast indicates that the ionic migration in the SCI-FA_{0.91}Cs_{0.09}PbI₃ is much suppressed upon Cs sequential incorporation.

Suppressed ionic migration in SCI-FA_{0.91}Cs_{0.09}PbI₃ is consistent with suppressed electron-phonon coupling upon Cs incorporation. Figure 4e shows the full-width half-maximum (FWHM) of the PL peak of SCI-FA_{0.91}Cs_{0.09}PbI₃ and FAPbI₃ perovskites (Supplementary Fig. 16) ranging from 110 to 296 K. The wide broadening of the PL linewidth in FAPbI₃ perovskites arises from strong electron-phonon coupling [35,36]. The electron-phonon interaction is dominated by high energy longitudinal optical (LO) phonons in the high-temperature region, where the measured FWHM data could be fitted by the Boson model (Fig. 4c, Supplementary Fig. 18 and Supplementary Table 3). Compared with FAPbI₃, both the electron-LO phonon coupling coefficient (Γ_{LO}) and LO phonon energy ($\hbar\omega$) in the SCI-FA_{0.91}Cs_{0.09}PbI₃ are significantly reduced, indicating that the fluctuation of the PbI₆ octahedra cage in SCI-FA_{0.91}Cs_{0.09}PbI₃ is associated with much smaller energies upon the Cs sequential incorporation. This is consistent with the previous theoretical investigations, which indicate that mixed A-site cations could reduce the lattice fluctuations in halide perovskites [37]. As such, the suppressed lattice fluctuations and electron-phonon coupling in SCI-FA_{0.91}Cs_{0.09}PbI₃ rationalize suppressed ionic migration and hence enhanced stability in SCI-FA_{0.91}Cs_{0.09}PbI₃ PSCs, which agree with previous research results that the suppressed lattice fluctuations and reduced electron-phonon coupling could suppress the formation of iodide-rich clusters to improve the stability of halide perovskites [38,39].

CONCLUSION

In summary, we successfully develop a novel SCI strategy to tackle the critical challenge of different crystallization dynamics of different cations in developing FA_{1-x}Cs_xPbI₃ perovskite PSCs. The resulting pure iodide SCI-FA_{1-x}Cs_xPbI₃ perovskites show more uniform composition distribution and reduced defects/traps density than FAPbI₃ and one-step crystallized 1S-FA_{0.91}Cs_{0.09}PbI₃. Compared with FAPbI₃, the SCI-FA_{0.91}Cs_{0.09}PbI₃ exhibits reduced electron-phonon coupling and lattice fluctuations, minimizing ion migration and hence enhancing the stability. As such, we have been able to achieve highly stable PSCs with a high efficiency of 24.7%, which is a record for SCI-FA_{1-x}Cs_xPbI₃ PSCs. This work opens up new possibilities to develop high-quality

mixed-cation perovskites, presenting a milestone towards the development of highly efficient and highly stable perovskites for various applications, including solar cells, light-emitting diodes and lasers.

METHODS

Materials

Lead iodide (PbI_2 , 99.9985%), cesium formate (HCOOCs , 98%), methylamine hydrochloride (MACl , 99%) and tin (IV) oxide colloid precursor (SnO_2 , 15% in H_2O colloidal dispersion) were purchased from Alfa Aesar. Formamidinium iodide (FAI) was purchased from Xi'an Polymer Light Technology Corp. Other materials were purchased from Sigma-Aldrich and used as received without any purification. *N,N*-dimethylformamide (DMF, anhydrous, 99.8%), dimethyl sulfoxide (DMSO, anhydrous, 99.7%), chlorobenzene (anhydrous, 99.8%) and isopropanol alcohol (IPA, 99.5%) were purchased from J&K Scientific Ltd. Ammonium solution (AR, 25%–28%) was purchased from Aladdin.

Device fabrication

A compact TiO_2 layer (20 nm) was deposited using the spray pyrolysis method using a titanium bis(ethyl acetoacetate)-diisopropoxide/1-butanol solution (1 : 9 volume ratio). The cleaned patterned fluorine-doped tin oxide (FTO, $7 \Omega \text{ sq}^{-1}$) substrate was placed on a 450°C plate during the spray process followed by 1 h of annealing. The SnO_2 colloid precursor/ammonium solution (1 : 9 volume ratio) was spin-coated on a TiO_2 layer at 3000 rpm for 30 s followed by annealing for 30 min at 180°C . The $\text{SCI-FA}_{1-x}\text{Cs}_x\text{PbI}_3$ perovskite precursor was prepared by mixing PbI_2 , FAI and MACl (30 mol%) in $\text{DMF} : \text{DMSO} = 9:1$ solution to form 1.5 M FAPbI_3 precursor. The perovskite precursor films were deposited by spin-coating on $\text{FTO}/\text{TiO}_2/\text{SnO}_2$ substrate at 5000 rpm for 15 s. During spin-coating, 150–200 μL of chlorobenzene was dripped at the end of 10 s. For the SCI perovskite samples, the perovskite film was first annealed for 1 min at 150°C to obtain a light-brown FA perovskite film. Different concentrations of HCOOCs/IPA solution were dropped on the FAPbI_3 precursor films then spin-coated at 3000 rpm for 30 s and further annealed at 150°C for 9 min and 100°C for 10 min. The $1\text{S-FA}_{1-x}\text{Cs}_x\text{PbI}_3$ perovskite was prepared by mixing PbI_2 , FAI, MACl (30 mol%) and x mol% HCOOCs in $\text{DMF} : \text{DMSO} = 9:1$ solution to form 1.5 M FA-Cs precursor. The perovskite precursor films were deposited by spin-coating on $\text{FTO}/\text{TiO}_2/\text{SnO}_2$ substrate at

5000 rpm for 15 s. During spin-coating, 150–200 μL of chlorobenzene was dripped at the end of 10 s. The perovskite films annealed at 150°C for 10 min and 100°C for 10 min. The spiro-OMeTAD layer was spin-coated by dissolving 90 mg of spiro-OMeTAD in 1 mL of chlorobenzene and mixing with 39.5 μL of 4-*tert*-butylpyridine (TBP), 23 μL of Li-bis(trifluoromethanesulfonyl) imide (Li-TFSI)/acetonitrile (520 mg/mL) and 10 μL of tris(2-(1*h*-pyrazol-1-yl)-4-*tert*-butylpyridine)-cobalt(III)tris(bis(trifluoromethylsulfonyl)imide) (FK209)/acetonitrile (375 mg mL^{-1}) at 4000 rpm for 25 s. Finally, a 80-nm thick gold electrode was thermal evaporated on the spiro-OMeTAD layer. The perovskite films fabrication was operated in a dry box with <15% humidity.

SUPPLEMENTARY DATA

Supplementary data are available at [NSR](https://doi.org/10.1093/nsr/nwac127) online.

ACKNOWLEDGEMENTS

We thank the Instrumental Analysis Center (School of Environmental Science and Engineering, Shanghai Jiao Tong University) for assistance with material characterization tests. We thank the Shanghai Synchrotron Radiation Facility (SSRF) for assistance with GIWAXS measurements. We also thank the National Institute of Metrology (China) for authentication tests.

FUNDING

The work performed at Shanghai Jiao Tong University was supported by the National Natural Science Foundation of China (22025505) and the Program of Shanghai Academic/Technology Research Leader (20XD1422200). The work performed at the Linköping University was supported by the Swedish Government Strategic Research Area in Materials Science on Functional Materials at Linköping University (SFO-Mat-LiU #2009–00971).

AUTHOR CONTRIBUTIONS

Y.Z. and F.G. designed and directed the study. H.C. and Y.F. conceived and performed the device fabrication work. Y.W. performed photophysical measurements and analysed the results. H.C., Y.F., Y.W., Y.C., Y.M., Z.Q., X.W., X.L., K.Z., F.G. and Y.Z. participated in characterization and data analysis. All authors contributed to the discussions. H.C., Y.F., Y.W., F.G. and Y.Z. wrote the manuscript with input from all authors. All authors reviewed the paper.

Conflict of interest statement. None declared.

REFERENCES

1. Kojima A, Teshima K and Shirai Y *et al.* Organometal halide perovskites as visible-light sensitizers for photovoltaic cells. *J Am Chem Soc* 2009; **131**: 6050–1.

2. Kim H-S, Lee C-R and Im J-H *et al.* Lead iodide perovskite sensitized all-solid-state submicron thin film mesoscopic solar cell with efficiency exceeding 9%. *Sci Rep* 2012; **2**: 591.
3. Lee MM, Teuscher J and Miyasaka T *et al.* Efficient hybrid solar cells based on meso-superstructured organometal halide perovskites. *Science* 2012; **338**: 643–7.
4. Xu W, Hu Q and Bai S *et al.* Rational molecular passivation for high-performance perovskite light-emitting diodes. *Nat Photon* 2019; **13**: 418–24.
5. Karlsson M, Yi Z and Reichert S *et al.* Mixed halide perovskites for spectrally stable and high-efficiency blue light-emitting diodes. *Nat Commun* 2021; **12**: 361.
6. Veldhuis SA, Boix PP and Yantara N *et al.* Perovskite materials for light-emitting diodes and lasers. *Adv Mater* 2016; **28**: 6804–34.
7. Eperon GE, Stranks SD and Menelaou C *et al.* Formamidinium lead trihalide: a broadly tunable perovskite for efficient planar heterojunction solar cells. *Energy Environ Sci* 2014; **7**: 982–8.
8. Lu H, Liu Y and Ahlawat P *et al.* Vapor-assisted deposition of highly efficient, stable black-phase FAPbI₃ perovskite solar cells. *Science* 2020; **370**: eabb8985.
9. Hui W, Chao L and Lu H *et al.* Stabilizing black-phase formamidinium perovskite formation at room temperature and high humidity. *Science* 2021; **371**: 1359–64.
10. Koh TM, Fu K and Fang Y *et al.* Formamidinium-containing metal-halide: an alternative material for near-IR absorption perovskite solar cells. *J Phys Chem C* 2014; **118**: 16458–62.
11. Weller MT, Weber OJ and Frost J *et al.* Cubic perovskite structure of black formamidinium lead iodide, α -[HC(NH₂)₂]PbI₃, at 298 K. *J Phys Chem Lett* 2015; **6**: 3209–12.
12. Han Q, Bae S-H and Sun P *et al.* Single crystal formamidinium lead iodide (FAPbI₃): insight into the structural, optical, and electrical properties. *Adv Mater* 2016; **28**: 2253–8.
13. Chen T, Foley BJ and Park C *et al.* Entropy-driven structural transition and kinetic trapping in formamidinium lead iodide perovskite. *Sci Adv* 2016; **2**: e1601650.
14. Rehman W, McMeekin DP and Patel JB *et al.* Photovoltaic mixed-cation lead mixed-halide perovskites: links between crystallinity, photo-stability and electronic properties. *Energy Environ Sci* 2017; **10**: 361–9.
15. Turren-Cruz S-H, Hagfeldt A and Saliba M. Methylammonium-free, high-performance, and stable perovskite solar cells on a planar architecture. *Science* 2018; **362**: 449–53.
16. Lee J-W, Kim D-H and Kim H-S *et al.* Formamidinium and cesium hybridization for photo- and moisture-stable perovskite solar cell. *Adv Energy Mater* 2015; **5**: 1501310.
17. Li Z, Yang M and Park J-S *et al.* Stabilizing perovskite structures by tuning tolerance factor: formation of formamidinium and cesium lead iodide solid-state alloys. *Chem Mater* 2016; **28**: 284–92.
18. Yi C, Luo J and Meloni S *et al.* Entropic stabilization of mixed A-cation ABX₃ metal halide perovskites for high performance perovskite solar cells. *Energy Environ Sci* 2016; **9**: 656–62.
19. Deng Y, Xu S and Chen S *et al.* Defect compensation in formamidinium-caesium perovskites for highly efficient solar mini-modules with improved photostability. *Nat Energy* 2021; **6**: 633–41.
20. Zhang T, Chen Y and Kan M *et al.* MA cation-induced diffusional growth of low-bandgap FA-Cs perovskites driven by natural gradient annealing. *Research* 2021; **2021**: 9765106.
21. Li N, Luo Y and Chen Z *et al.* Microscopic degradation in formamidinium-cesium lead iodide perovskite solar cells under operational stressors. *Joule* 2020; **4**: 1743–58.
22. Kim G, Min H and Lee K-S *et al.* Impact of strain relaxation on performance of α -formamidinium lead iodide perovskite solar cells. *Science* 2020; **370**: 108–12.
23. Yang J, Chen Y and Tang W *et al.* Crystallization tailoring of cesium/formamidinium double-cation perovskite for efficient and highly stable solar cells. *J Energy Chem* 2020; **48**: 217–25.
24. Wang Z, Lin Q and Chmiel FP *et al.* Efficient ambient-air-stable solar cells with 2D–3D heterostructured butylammonium-caesium-formamidinium lead halide perovskites. *Nat Energy* 2017; **2**: 17135.
25. Yang G, Ren Z and Liu K *et al.* Stable and low-photovoltage-loss perovskite solar cells by multifunctional passivation. *Nat Photon* 2021; **15**: 681–9.
26. Zheng X, Wu C and Jha SK *et al.* Improved phase stability of formamidinium lead triiodide perovskite by strain relaxation. *ACS Energy Lett* 2016; **1**: 1014–20.
27. Seo J-Y, Matsui T and Luo J *et al.* Ionic liquid control crystal growth to enhance planar perovskite solar cells efficiency. *Adv Mater* 2016; **6**: 1600767.
28. Jeong J, Kim M and Seo J *et al.* Pseudo-halide anion engineering for α -FAPbI₃ perovskite solar cells. *Nature* 2021; **592**: 381–5.
29. Jiang Q, Zhao Y and Zhang X *et al.* Surface passivation of perovskite film for efficient solar cells. *Nat Photon* 2019; **13**: 460–6.
30. Tress W, Marinova N and Inganäs O *et al.* Predicting the open-circuit voltage of CH₃NH₃PbI₃ perovskite solar cells using electroluminescence and photovoltaic quantum efficiency spectra: the role of radiative and non-radiative recombination. *Adv Mater* 2015; **5**: 1400812.
31. Bube RH. Trap density determination by space-charge-limited currents. *J Appl Phys* 1962; **33**: 1733–7.
32. Yang D, Yang R and Wang K *et al.* High efficiency planar-type perovskite solar cells with negligible hysteresis using EDTA-complexed SnO₂. *Nat Commun* 2018; **9**: 3239.
33. Wang Y, Dar MI and Ono Luis K *et al.* Thermodynamically stabilized β -CsPbI₃-based perovskite solar cells with efficiencies >18%. *Science* 2019; **365**: 591–5.
34. Wang X, Wang Y and Chen Y *et al.* Efficient and stable CsPbI₃ inorganic perovskite photovoltaics enabled by crystal secondary growth. *Adv Mater* 2021; **33**: 2103688.
35. Guo Z, Wu X and Zhu T *et al.* Electron–phonon scattering in atomically thin 2D perovskites. *ACS Nano* 2016; **10**: 9992–8.
36. Gong X, Voznyy O and Jain A *et al.* Electron–phonon interaction in efficient perovskite blue emitters. *Nat Mater* 2018; **17**: 550–6.
37. Ghosh D, Walsh Atkins P and Islam MS *et al.* Good vibrations: locking of octahedral tilting in mixed-cation iodide perovskites for solar cells. *ACS Energy Lett* 2017; **2**: 2424–9.
38. deQuilettes DW, Zhang W and Burlakov VM *et al.* Photo-induced halide redistribution in organic–inorganic perovskite films. *Nat Commun* 2016; **7**: 11683.
39. Bischak CG, Hetherington CL and Wu H *et al.* Origin of reversible photoinduced phase separation in hybrid perovskites. *Nano Lett* 2017; **17**: 1028–33.